Chemical Science

ROYAL SOCIETY OF CHEMISTRY

EDGE ARTICLE

View Article Online
View Journal

Open Access Article. Published on 24 April 2026. Downloaded on 5/16/2026 10:23:42 PM.
This article is licensed under a Creative Commons Attribution-NonCommercial 3.0 Unported Licence.

Check for updates

Cite this: DOI: 10.1039/d6sc01756h

All publication charges for this article have been paid for by the Royal Society of Chemistry

Received 2nd March 2026
Accepted 23rd April 2026

DOI: 10.1039/d6sc01756h

rsc.li/chemical-science

High-capacity sieving of C_3F_6 and C_3F_8 by a copper-based MOF with interconnected gourd-shaped channels

Zijian Wang,[ab] Mu-Yang Zhou,[b] Shanshan Mao,[b] Yilu Wu,[b] Shenfang Li,[ab] Xin Zhou,[b] Fu-An Guo,[ab] Liang Yu,*[b] Manglai Gao*[ac] and Hao Wang *[b]

Targeting the challenging purification of electronic-grade C_3F_8, we report the size-sieving separation of C_3F_6 and C_3F_8 by a robust copper-based metal–organic framework, **CuHTPO**, that features a distinctive interconnected "gourd"-shaped pore architecture. This compound completely excludes C_3F_8 while strongly adsorbing C_3F_6, achieving an adsorption capacity as high as 71.3 $cm^3\ g^{-1}$ at 298 K and 100 kPa. Dynamic breakthrough experiments demonstrate the direct production of ultra-high-purity C_3F_8 (>5N) from a C_3F_6/C_3F_8 (10 : 90, v/v) gas mixture. The underlying size-sieving-based separation mechanism is corroborated by *in situ* infrared spectroscopy and density functional theory calculations.

Introduction

Perfluoropropane (C_3F_8), owing to its unique carbon-to-fluorine ratio (C/F = 0.375) and favorable thermodynamic properties, exhibits an excellent process window in HARC (high aspect ratio contact) etching and CVD (chemical vapor deposition) chamber cleaning.[1] However, as process nodes approach near-zero defect tolerance, the purity requirement for C_3F_8 has been elevated to above 99.999% (5N).[2–5] Beyond the electronics industry, C_3F_8 plays an irreplaceable role in the medical field particularly in complex vitreoretinal surgeries, where similarly stringent purity standards are required.[6] The presence of any toxic impurities may lead to irreversible damage to the retinal neuroepithelium or unintended elevation of intraocular pressure,[7,8] potentially resulting in severe clinical complications. C_3F_6 is one of the most ubiquitous impurities encountered during both industrial purification and exhaust gas recovery of C_3F_8.[9–13] Owing to the small boiling point difference between C_3F_6 and C_3F_8 ($\Delta T_b \approx 7.3$ K), achieving >5N purity *via* cryogenic distillation requires exceptionally high reflux ratios and oversized distillation columns, resulting in prohibitive energy consumption and capital costs.[14–16] Consequently, the development of efficient and low-energy separation strategies for C_3F_6 removal from C_3F_8 is of critical industrial importance.

Adsorptive separation utilizing porous materials has emerged as a compelling alternative to cryogenic distillation, driven by its superior energy efficiency and lower capital expenditure.[17] Conventional adsorbents, exemplified by activated carbon and zeolites, have demonstrated the potential for physical discrimination of C_3F_6 and C_3F_8.[18–23] Metal–organic frameworks (MOFs), exhibiting remarkable tunability in pore size, topology, and surface chemistry, hold particularly promise for precise separation of physicochemically similar molecules.[24–31] Given the ultrahigh purity requirement of electronic-grade C_3F_8, molecular sieving is widely considered the most desirable separation mechanism for removing trace C_3F_6 and directly producing high-purity C_3F_8. However, achieving precise size-dependent discrimination is frequently accompanied by a significant reduction in adsorption capacity. Recent strategies involving framework flexibility,[31,32] pore environment engineering,[33,34] electrostatic modulation,[35] and biomimetic design[36] have largely mitigated this limitation, nevertheless, sieving-based MOFs with high adsorption capacity remains highly needed.

In this work, we demonstrate high-capacity sieving of C_3F_6 and C_3F_8 using a MOF featuring large cages accessible through narrow windows. This architecture allows for the maximal packing of guest molecules within the internal voids while maintaining strictly defined apertures for size-selective discrimination.[37–42] The robust copper-based MOF, **CuHTPO** (H_3TPO = tris-(4-carboxylphenyl) phosphine oxide), featuring interconnected "gourd"-shaped pore channels, effectively overcomes the "trade-off" between adsorption capacity and size-sieving precision. **CuHTPO** completely excludes C_3F_8 while its large internal cavities provide abundant adsorption sites for C_3F_6. As a result, it exhibits negligible uptake of C_3F_8 but a record-high C_3F_6 adsorption capacity of 71.3 $cm^3\ g^{-1}$ at 298 K

[a]*State Key Laboratory of Heavy Oil Processing, College of Science, China University of Petroleum, Beijing 102249, P. R. China. E-mail: mlgao@cup.edu.cn*

[b]*Hoffmann Institute of Advanced Materials, Shenzhen Polytechnic University, 7098 Liuxian Blvd., Nanshan District, Shenzhen, Guangdong 518055, P. R. China. E-mail: yuliang@szpu.edu.cn; wanghao@szpu.edu.cn*

[c]*Liaoning Petrochemical University, No.1 West Section of Dandong Road, Wanghua District, Fushun City, Liaoning Province, 113001, China*

© 2026 The Author(s). Published by the Royal Society of Chemistry

Open Access Article. Published on 24 April 2026. Downloaded on 5/16/2026 10:23:42 PM. This article is licensed under a Creative Commons Attribution-NonCommercial 3.0 Unported Licence.

and 100 kPa. Dynamic breakthrough experiments further demonstrate the direct production of high-purity C_3F_8 (>5N) from a C_3F_6/C_3F_8 (10 : 90, v/v) mixture with excellent cycling stability, while *in situ* infrared spectroscopy and density functional theory calculations provide insight into the underlying separation mechanism.

Results and discussion

CuHTPO was synthesized *via* a slightly modified procedure based on a previously reported method,[43] with detailed synthetic protocols provided in the SI. Briefly, $Cu(NO_3)_2 \cdot 3H_2O$ and H_3TPO were subjected in a mixed solvent of *N*,*N*-dimethylformamide/H_2O/methanol, and the subsequent solvothermal reaction afforded crystals of **CuHTPO** (Fig. S1 and S2). It crystallizes in the orthorhombic crystal system with the space group *Pbcn*. The framework is constructed from phosphine oxide ligand $HTPO^{2-}$ coordinated to classical paddlewheel-type $Cu_2(COO)_4$ secondary building units (SBUs) (Fig. 1a). Each $HTPO^{2-}$ ligand laterally bridges two copper clusters through two carboxylate groups, while a phosphine oxide moiety coordinates monodentately to a copper center along the axial direction; notably, the non-coordinated carboxylic acid groups engage in hydrogen-bonding interactions with carboxylate groups from neighboring ligands (Fig. 1b). **CuHTPO** assembles into a robust three-dimensional network, featuring pore channels extending along the a axis that exhibit a characteristic gourd-like architecture composed of alternating large cavities of approximately 6.9 Å and narrow pore apertures of about 5.5 Å (Fig. 1c). Distinct from conventional one-dimensional gourd-shaped channels,[44,45] the pores of **CuHTPO** form a two-dimensional interconnected "gourd"-shaped channel system propagating along the ac plane, in which large cavities are interconnected by four narrow apertures (Fig. 1d). This unique pore topology not only mitigates the intrinsic trade-off between selectivity and adsorption capacity in molecular sieving but also provides multiple and efficient diffusion pathways for guest molecules within the framework.

The phase purity of as-synthesized **CuHTPO** was confirmed by powder X-ray diffraction (PXRD). As shown in Fig. S3, the PXRD patterns of the as-synthesized and methanol-exchanged samples match well with the simulated pattern derived from single-crystal data. Notably, the activated sample and the sample after adsorption measurements retain identical diffraction features, indicating full preservation of crystallinity throughout activation and adsorption processes. Thermogravimetric analysis (TGA) of the as-synthesized sample reveals continuous mass loss upon heating, whereas the methanol-exchanged sample exhibits an extended plateau up to 320 °C (Fig. S4). Furthermore, the chemical and thermal stability of **CuHTPO** were systematically investigated. The material was immersed in various organic solvents and aqueous solutions with pH values ranging from 3 to 9 for seven days. PXRD analyses reveal that the framework structure is largely preserved in different organic solvents (Fig. S5), while maintaining good structural integrity in mildly acidic aqueous media (Fig. S6).

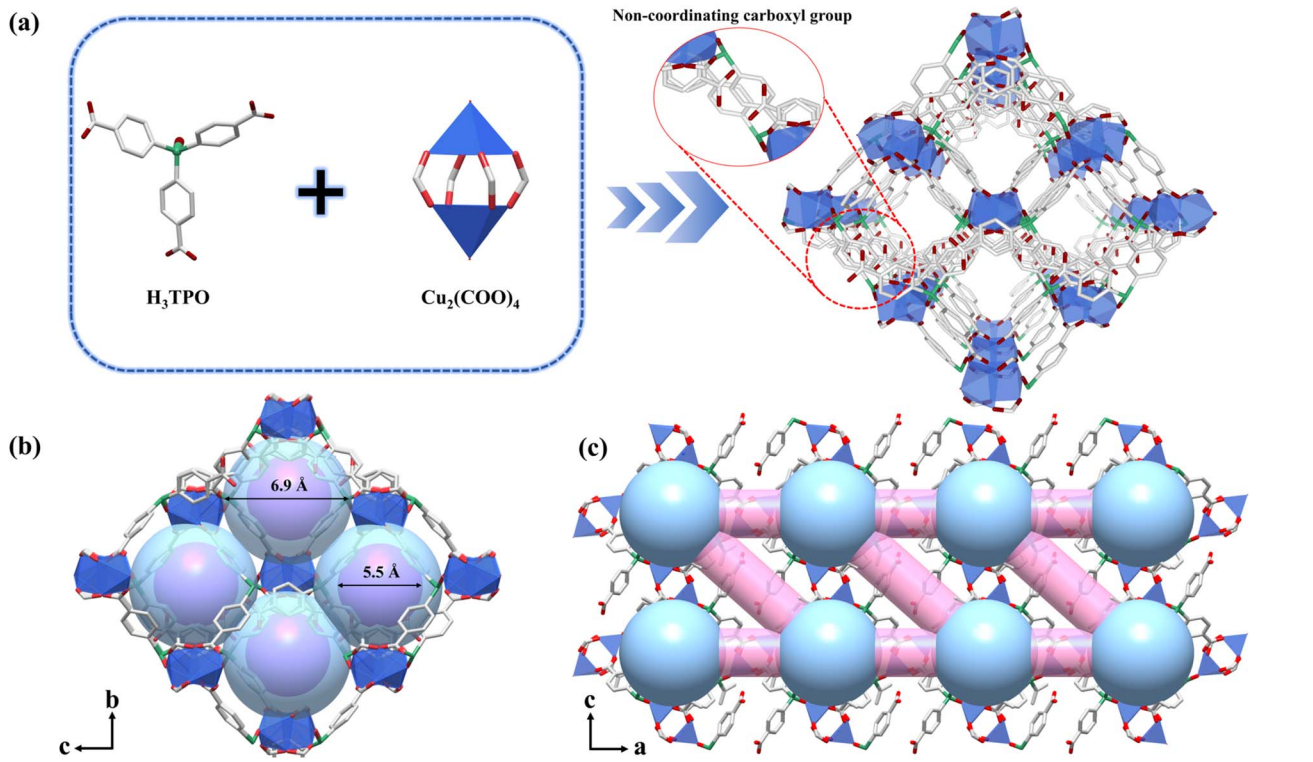

Fig. 1 Crystal structure of **CuHTPO**. (a) 3D structure built from H_3TPO and $Cu_2(COO)_4$. (b and c) Cavities and 2D channels of **CuHTPO**. Color scheme: Cu, blue; O, red; C, gray; P green.

© 2026 The Author(s). Published by the Royal Society of Chemistry

Open Access Article. Published on 24 April 2026. Downloaded on 5/16/2026 10:23:42 PM. This article is licensed under a Creative Commons Attribution-NonCommercial 3.0 Unported Licence.

This stability is particularly relevant considering that industrial production of C_3F_8 typically introduces trace amounts of acidic impurities,[46] rendering the crude product weakly acidic. Therefore, materials exhibiting resistance to mildly acidic environments are better suited for practical separation processes in such systems. In addition, variable-temperature *in situ* PXRD measurements under a nitrogen atmosphere demonstrate that the crystalline structure of **CuHTPO** remains essentially intact up to 320 °C (Fig. S7). Combined with its stability in various solvents, this robustness enables the use of more rigorous yet efficient solvent-exchange and activation procedures. The permanent porosity of **CuHTPO** was evaluated by N_2 adsorption at 77 K, revealing two types of pores with diameters of 5.5 and 6.8 Å, respectively (Fig. 2a and S8), in good agreement with the crystal structure. The adsorption displays an N_2 uptake of 239 $cm^3\ g^{-1}$, and a corresponding Brunauer–Emmett–Teller (BET) surface area of 1000.3 $m^2\ g^{-1}$ (Fig. S9).

The robust framework and precisely defined pore dimensions of **CuHTPO** prompted us to evaluate its adsorption and separation performance toward C_3F_6 and C_3F_8. Single-component adsorption isotherms for C_3F_6 and C_3F_8 were measured at 273, 298, and 308 K (Fig. 2b). Across this temperature range, **CuHTPO** exhibits negligible adsorption of C_3F_8, whereas a typical type-I adsorption profile is observed for C_3F_6. At 298 K and 100 kPa, **CuHTPO** delivers a substantial C_3F_6 uptake of 71.6 $cm^3\ g^{-1}$ (3.2 mmol g^{-1}). These results clearly demonstrate that **CuHTPO** is capable of completely excluding the bulkier C_3F_8 while efficiently adsorbing C_3F_6, highlighting its potential for purifying C_3F_8 by removing trace C_3F_6. Notably, the C_3F_6 adsorption capacity of **CuHTPO** surpasses previously reported molecular-sieving-based benchmark MOFs for C_3F_6/C_3F_8 separation, including Ca-tcpb[31] (44.8 $cm^3\ g^{-1}$), Ni(INA)$_2$-NH_2 (ref. 33) (56.7 $cm^3\ g^{-1}$), Zr-PMA[34] (59.1 $cm^3\ g^{-1}$), Zn-bzx-CF_3 (ref. 35) (47.0 $cm^3\ g^{-1}$), and CoFA[36] (44.8 $cm^3\ g^{-1}$) (Fig. 2d and Table S3). Adsorption kinetics measurements reveal that **CuHTPO** takes up C_3F_6 quickly, whereas C_3F_8 remains essentially being excluded, confirming its selective molecular exclusion behavior (Fig. 2c). The calculated diffusion time constant for C_3F_6 ($3.3 \times 10^{-3}\ s^{-1}$) surpasses that of C_3F_8 ($6.4 \times 10^{-5}\ s^{-1}$) by a factor of over 50 (Fig. S10). We attribute this precise size-sorting to the optimal pore window of the large-cavity-small-aperture architecture of **CuHTPO**.

To quantitatively evaluate the binding strength of C_3F_6 and C_3F_8 within the **CuHTPO** framework, differential scanning calorimetry (DSC) measurements were performed at 298 K. The adsorption enthalpy (ΔH_{ads}) for C_3F_6 was determined to be 43.02 kJ mol^{-1}, whereas the value for C_3F_8 was negligible (Fig. 3a). Furthermore, the isosteric heat of adsorption (Q_{st})

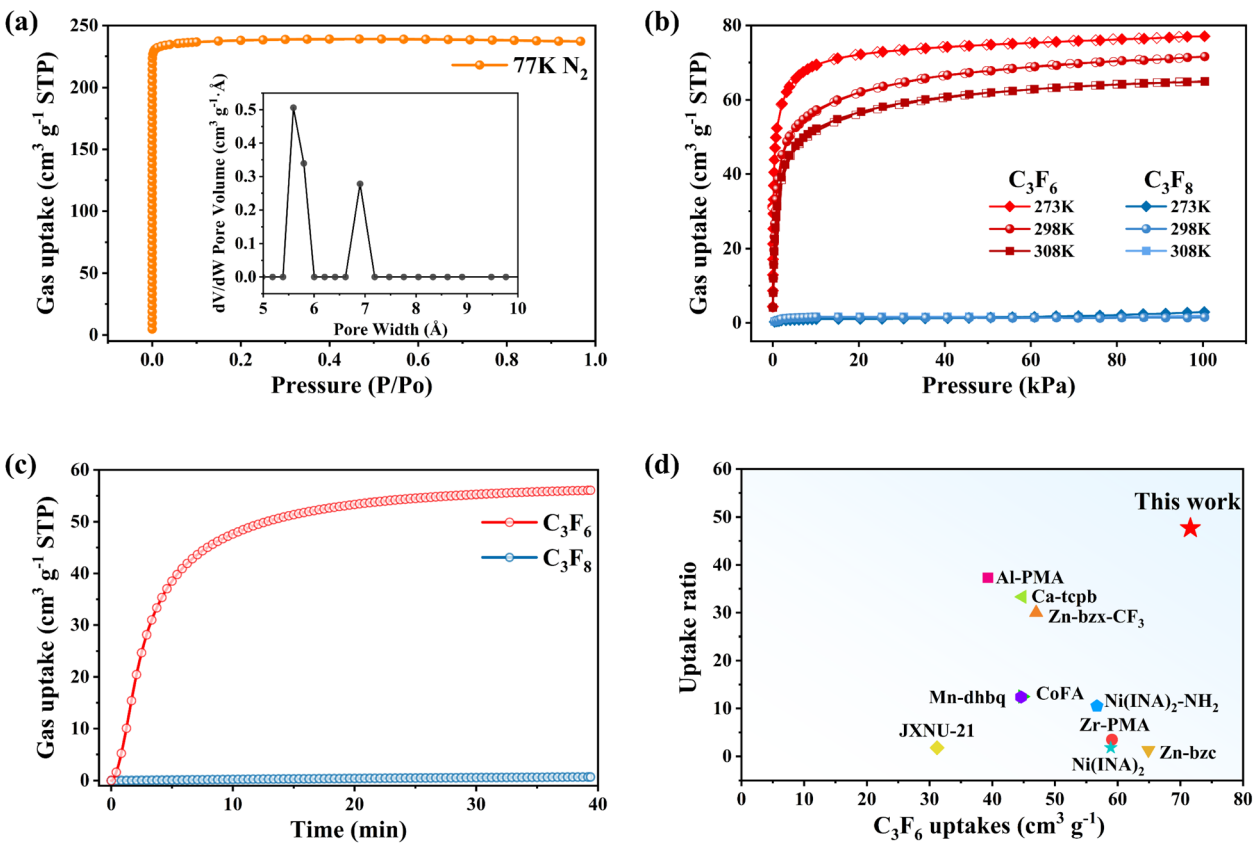

Fig. 2 (a) N_2 adsorption isotherms of **CuHTPO** measured at 77 K (inset: pore size distribution derived from the DFT method). (b) Single-component adsorption isotherms of C_3F_6 and C_3F_8 on **CuHTPO** measured at different temperatures. (c) Adsorption kinetics of C_3F_6 and C_3F_8 obtained at 298 K and a partial pressure of 0.5 bar. (d) Comparison of the C_3F_6/C_3F_8 uptake ratio and the C_3F_6 uptake at 298 K and 100 kPa for **CuHTPO** and representative benchmark material.

Open Access Article. Published on 24 April 2026. Downloaded on 5/16/2026 10:23:42 PM.
This article is licensed under a Creative Commons Attribution-NonCommercial 3.0 Unported Licence.

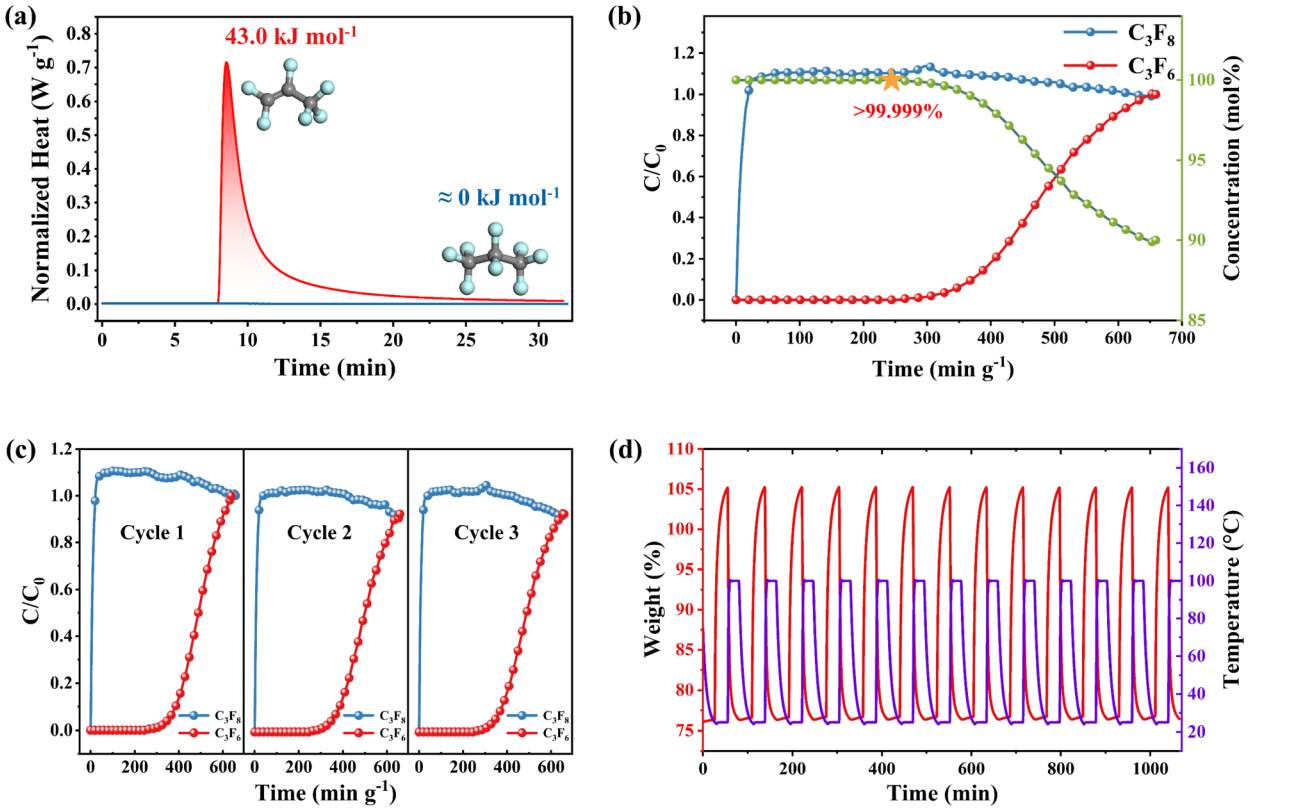

Fig. 3 (a) Differential scanning calorimetry (DSC)-derived adsorption enthalpies of **CuHTPO** toward C_3F_6 and C_3F_8. (b) Binary breakthrough curves of a C_3F_6/C_3F_8 (10 : 90, v/v) mixture recorded at 298 K using a fixed-bed column packed with **CuHTPO**; The purity of C_3F_8 exceeded 99.999% before the breakthrough of C_3F_6. (c) Comparison of three consecutive dynamic separation cycles. (d) C_3F_6 adsorption–desorption cycling performance of **CuHTPO** over 10 consecutive cycles at 298 K.

calculated from the C_3F_6 isotherms at various temperatures is ≈38.7 kJ mol^{-1} (Fig. S11–S16), generally matching the adsorption enthalpy measured by DSC. On this basis, the dynamic separation performance of **CuHTPO** toward the C_3F_6/C_3F_8 mixture was further evaluated at 298 K using a fixed-bed column packed with **CuHTPO** under a feed composition of C_3F_6/C_3F_8 (10 : 90, v/v). As shown in Fig. 3b, C_3F_8 eluted immediately upon introduction of the gas mixture, whereas C_3F_6 was retained in the column and did not break through until approximately 240 min g^{-1}, thereby enabling the production of ultrapure C_3F_8 (>99.999%) with a high yield of 323.65 cm^3 g^{-1}. Furthermore, subsequent adsorption–desorption breakthrough cycling experiments, in which the column was regenerated under a He flow at 423 K, revealed nearly identical breakthrough profiles over three consecutive cycles (Fig. 3c), demonstrating the excellent recyclability and cycling stability of **CuHTPO**.

In addition, to systematically assess its long-term recyclability, temperature-swing adsorption–desorption cycling tests were conducted, during which the sample was exposed to pure C_3F_6 at 298 K followed by regeneration under an N_2 atmosphere at 373 K. Notably, no discernible loss in uptake capacity was observed over 10 consecutive cycles (Fig. 3d), highlighting the structural stability and reusability of **CuHTPO**.

To gain deeper insights into the adsorption mechanism of perfluorinated gases within the **CuHTPO** framework, *in situ* infrared (IR) spectroscopy measurements were performed (Fig. 4a and b). Upon activation, approximately 20 Torr of pure C_3F_6 or C_3F_8 was introduced into the IR cell, and difference spectra at various time intervals were obtained by subtracting the activated-state spectrum from the adsorption spectra. As shown in Fig. 4a and b, upon introduction of C_3F_6, a red shift of approximately 5 cm^{-1} was observed in the 1193–1178 cm^{-1} region, which can be assigned to the asymmetric C–F stretching vibration (ν_{as}) of C_3F_6, while a distinct negative band appears around 1000 cm^{-1}, attributed to the in-plane bending vibration of aromatic C–H (δ), indicating that this mode is sensitive to guest occupancy and suggesting the presence of specific host–guest interactions dominated by C–H···F hydrogen bonding between C_3F_6 and the framework; in contrast, upon exposure to C_3F_8, no significant changes were observed in the aromatic C–H in-plane deformation region and only gas-phase C–F vibrational features were detected near 1000 cm^{-1} These results directly demonstrate, at the molecular level, that **CuHTPO** discriminates C_3F_6 from C_3F_8 through a molecular sieving mechanism.

Density functional theory (DFT) calculations further corroborated the conclusions drawn from the *in situ* IR experiments. As illustrated in Fig. 4c, C_3F_6 preferentially resides in the corner regions of the pore, where the dominant interactions arise from multiple C–F···H hydrogen bonds formed between fluorine atoms of C_3F_6 and hydrogen atoms on the phenyl rings

© 2026 The Author(s). Published by the Royal Society of Chemistry

Open Access Article. Published on 24 April 2026. Downloaded on 5/16/2026 10:23:42 PM.
This article is licensed under a Creative Commons Attribution-NonCommercial 3.0 Unported Licence.

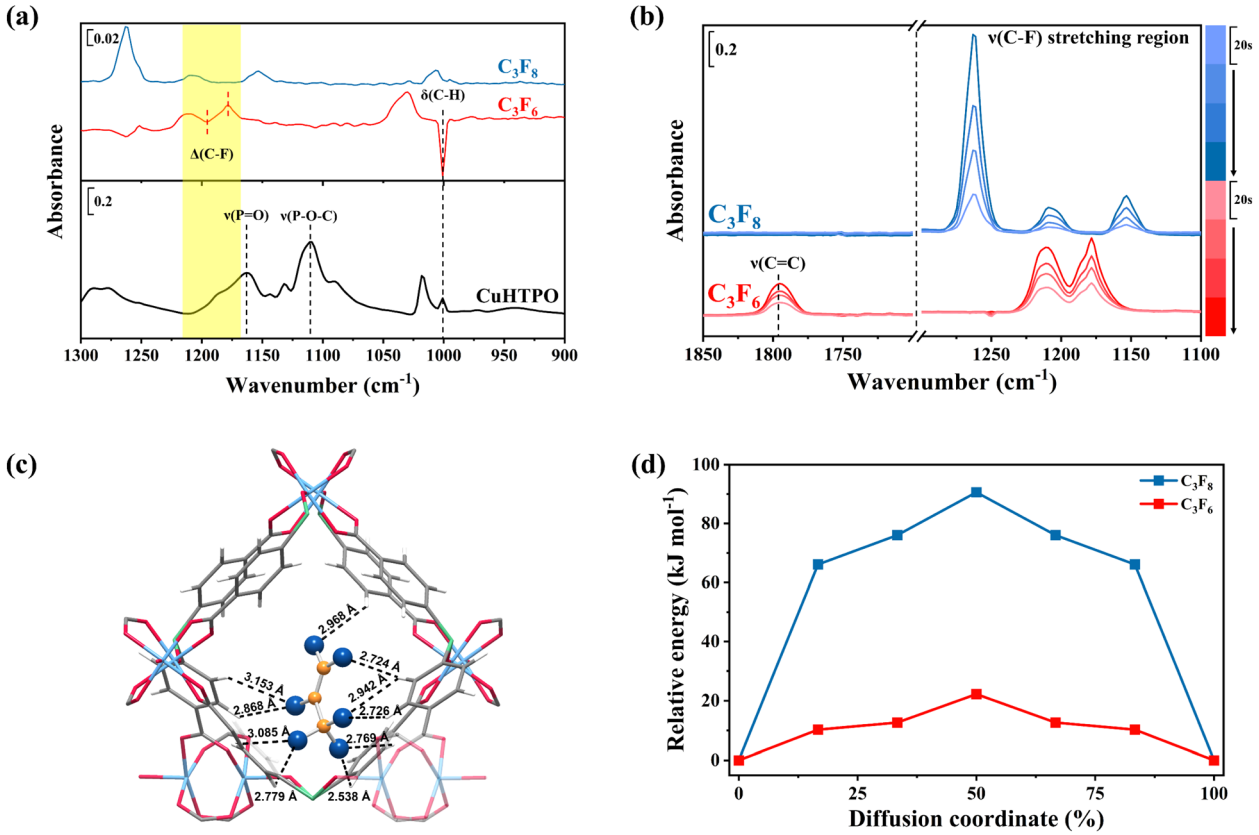

Fig. 4 IR difference spectra of **CuHTPO** upon loading C_3F_6 and C_3F_8 (≈20 Torr) at 298 K: (a) referenced to the activated sample under vacuum, with gas-phase signals subtracted and (b) time-resolved spectra collected at 20 min intervals. (c) The optimal adsorption sites of C_3F_6 on **CuHTPO**. (d) DFT-calculated energy profiles and relative energies for C_3F_6 and C_3F_8.

of the framework, with F···H interaction distances ranging from 2.538 to 3.153 Å (indicated by black dashed lines). To further validate the molecular sieving mechanism of **CuHTPO** toward C_3F_6 and C_3F_8, diffusion energy barrier calculations were performed. The calculated energy barrier for C_3F_6 is 22.2 kJ mol^{-1}, whereas that for C_3F_8 is as high as 90.6 kJ mol^{-1} (Fig. 4d), confirming that the diffusion of C_3F_8 is essentially prohibited. In addition, the calculated binding energy of C_3F_6 is 40.76 kJ mol^{-1}, which is in good agreement with the results obtained from DSC measurements. The charge density difference analysis reveals pronounced electron redistribution around the pore apertures and metal–ligand coordination sites upon C_3F_6 adsorption, indicating strong host–guest interactions accompanied by significant molecular polarization (Fig. S18). Consistently, electrostatic potential calculations show an overall positively charged framework and a negatively charged C_3F_6 molecule, confirming a favorable electrostatic affinity between the guest and the framework (Fig. S19). These theoretical results are in excellent agreement with the experimental adsorption behavior, further confirming that the optimal pore aperture of **CuHTPO** enables effective size-exclusive molecular sieving for C_3F_6/C_3F_8 separation.

Conclusions

We have demonstrated here the high-capacity size-sieving separation of C_3F_6 and C_3F_8 by a stable and robust copper-based metal–organic framework, **CuHTPO**. The unique coordination mode between the phosphine oxide-carboxylate ligand and copper nodes not only significantly enhances the structural stability of **CuHTPO**, but also constructs a distinctive interconnected "gourd"-shaped pore architecture, in which large cavities are connected through narrow pore apertures. This pore configuration effectively breaks the trade-off between selectivity and adsorption capacity commonly observed in conventional molecular-sieving MOFs, while simultaneously maintaining excellent framework robustness. Binary dynamic breakthrough experiments demonstrate that **CuHTPO** can stably produce ultra-high-purity C_3F_8 (>99.999%) over multiple cycles. Furthermore, *in situ* infrared spectroscopy combined with density functional theory calculations elucidates the interaction strengths of C_3F_6 and C_3F_8 within **CuHTPO** at the molecular level and reveals the underlying separation mechanism. This work provides important structure–performance relationship insights for the development of high-performance adsorbents for C_3F_6/C_3F_8 separation under stringent purity requirements.

© 2026 The Author(s). Published by the Royal Society of Chemistry

Open Access Article. Published on 24 April 2026. Downloaded on 5/16/2026 10:23:42 PM. This article is licensed under a Creative Commons Attribution-NonCommercial 3.0 Unported Licence.

Author contributions

H. Wang and L. Yu conceived and designed the project. M. Gao provided conceptual guidance. Z. Wang synthesized the compounds and performed PXRD analysis, stability tests, adsorption measurements, and breakthrough experiments. M.-Y. Zhou performed theoretical calculations. S. Li and X. Zhou provided technical support for the breakthrough tests. Y. Wu and F.-A. Guo conducted the *in situ* infrared spectroscopy experiments. Z. Wang, S. Mao, and L. Yu wrote the first draft of the manuscript. All authors contributed to the discussion of the results and the revision of the manuscript.

Conflicts of interest

There are no conflicts to declare.

Data availability

CCDC 2544357 contains the supplementary crystallographic data for this paper.[47]

Data associated to the article are available in the supplementary information (SI). Supplementary information: experimental methods, PXRD analysis, TGA curves, additional adsorption isotherms, calculation adsorption selectivity and heat for CuHTPO. See DOI: https://doi.org/10.1039/d6sc01756h.

Acknowledgements

This work was supported by the National Natural Science Foundation of China (22478251, 22508261), Guangdong Science and Technology Program (2024TQ08A672), Shenzhen Science and Technology Program (JCYJ20250604135818024), Shenzhen Polytechnic University Research Fund (6024310024K) and Postdoctoral Foundation of Shenzhen Polytechnic University (6024331002K).

Notes and references

1 K. Kim, C. Oh, N.-E. Lee, J. Kim, J. Bae, G. Yeom and S. Yoon, *J. Vac. Sci. Technol. B*, 2004, **22**, 483–488.
2 M. B. Chang and J.-S. Chang, *Ind. Eng. Chem. Res.*, 2006, **45**, 4101–4109.
3 F. Illuzzi, H. Thewissen and J. Integr, *Environ. Sci.*, 2010, **7**, 201–210.
4 W.-T. Tsai, H.-P. Chen and W.-Y. Hsien, *J. Loss Prev. Process Ind.*, 2002, **15**, 65–75.
5 R. S. Prabhakar, T. C. Merkel, B. D. Freeman, T. Imizu and A. Higuchi, *Macromolecules*, 2005, **38**, 1899–1910.
6 S. Chang, H. A. Lincoff, D. J. Coleman, W. Fuchs and M. E. Farber, *Ophthalmology*, 1985, **92**, 651–656.
7 N. C. Steinle, D. S. Dhoot, C. Q. Ruiz, A. A. Castellarin, D. J. Pieramici, R. F. See, S. C. Couvillion, M. a. A. Nasir and R. L. Avery, *Retina*, 2017, **37**, 643–650.
8 I. A. Rodrigues, A. N. Stangos, D. A. McHugh and T. L. Jackson, *Am. J. Ophthalmol.*, 2013, **155**, 270–276.
9 M. Basu, *Understanding Fluoride and Fluorocarbon Toxicity: An Overview*, Springer Nature Singapore, Singapore, 2024.
10 R. D. Chambers, *Fluorine in organic chemistry*, John Wiley & Sons, New York, 2004.
11 Y. Oda, R. Suzuki, T. Mori, H. Takahashi, H. Natsugari, D. Omata, J. Unga, H. Uruga, M. Sugii and S. Kawakami, *Int. J. Pharm.*, 2015, **487**, 64–71.
12 G. Casini, P. Loiudice, S. De Cillà, P. Radice and M. Nardi, *Int. J. Retina Vitreous*, 2016, **2**, 10.
13 S. M. McClintic, J. D. Grodsky and G. G. Emerson, *Retin. Physician*, 2025, **22**, 8–10.
14 X. Cao, R. Liu, Y. Lu, S. Jia and X. Yuan, *Sep. Purif. Technol.*, 2021, **279**, 119813.
15 D. S. Sholl and R. P. Lively, *Nature*, 2016, **532**, 435–437.
16 F. Fang and J. Joffe, *J. Chem. Eng. Data*, 1966, **11**, 376–379.
17 J.-R. Li, J. Sculley and H.-C. Zhou, *Chem. Rev.*, 2012, **112**, 869–932.
18 P. Hohenberg and W. Kohn, *Phys. Rev.*, 1964, **136**, B864.
19 W. Kohn and L. J. Sham, *Phys. Rev.*, 1965, **140**, A1133.
20 M. Menk, C. Bläker, C. Pasel and D. Bathen, *Microporous Mesoporous Mater.*, 2025, **402**, 113988.
21 Z. Du, Z. Wu, X. Li, W. Zhang, J. Huang, Y. Wu, L. Zhu and J. Xiao, *Sep. Purif. Technol.*, 2026, **383**, 136249.
22 Y. Fu, L. Sheng, W. Xia, G. Hai, J. Yan, L. Chen, Q. Yang, Z. Zhang, Q. Ren and Z. Bao, *Ind. Chem. Mater.*, 2025, **3**, 567–577.
23 X. Wei, S. Du, Y. Zheng, J. Peng, G. miao, X. Meng, X. Li, X. Li and J. Xiao, *AlChE J.*, 2026, **72**, e70155.
24 O. M. Yaghi and H. Li, *J. Am. Chem. Soc.*, 1995, **117**, 10401–10402.
25 B. M. Ji, D. Y. Zhang, R. Liang, G. H. Kang, Q. Y. Zhu and D. S. Deng, *Cryst. Growth Des.*, 2021, **21**, 482–489.
26 P. A. P. Mendes, P. Horcajada, S. Rives, H. Ren, A. E. Rodrigues, T. Devic, E. Magnier, P. Trens, H. Jobic, J. Ollivier, G. Maurin, C. Serre and J. A. C. Silva, *Adv. Funct. Mater.*, 2014, **24**, 7666–7673.
27 S. Kitagawa, *Chem. Soc. Rev.*, 2014, **43**, 5415–5418.
28 H. Furukawa, K. E. Cordova, M. O'Keeffe and O. M. Yaghi, *Science*, 2013, **341**, 1230444.
29 L. Lan, S. J. Wei, W. Xia, Q. Zhang, Y. Liu, C. Bao, M. Cheng, Z. Y. Qian, L. L. Wang, Y. L. Li, M. Feng, Z. Bao and T. L. Hu, *Angew Chem. Int. Ed. Engl.*, 2026, **72**, e6037453.
30 H.-F. Ma, X.-P. Fu, H.-P. Xiao, L. Chen, Q.-Y. Liu and Y.-L. Wang, *Sci. China Chem.*, 2026, DOI: 10.1007/s11426-025-3177-3.
31 W. Xia, Y. Yang, L. Sheng, Z. Zhou, L. Chen, Z. Zhang, Z. Zhang, Q. Yang, Q. Ren and Z. Bao, *Sci. Adv.*, 2024, **10**, eadj6473.
32 L. Sheng, W. Xia, Y. Fu, J. Yan, Z. Zhou, F. Zheng, F. Shen, L. Chen, Z. Zhang, Q. Yang, Q. Ren and Z. Bao, *ACS Mater. Lett.*, 2025, **7**, 2080–2087.
33 X. Lv, M. Zheng, Z. Jiang, H. Huang, Z. Bao and C. Zhong, *Chem. Eng. J.*, 2025, **522**, 168005.
34 W. Xia, Z. Zhou, C. Xia, L. Chen, L. Sheng, F. Zheng, Z. Zhang, Q. Yang, Q. Ren and Z. Bao, *Angew. Chem., Int. Ed.*, 2025, **64**, e202503505.

© 2026 The Author(s). Published by the Royal Society of Chemistry

Open Access Article. Published on 24 April 2026. Downloaded on 5/16/2026 10:23:42 PM.
This article is licensed under a Creative Commons Attribution-NonCommercial 3.0 Unported Licence.

35 M. Zheng, W. Xue, T. Yan, Z. Jiang, Z. Fang, H. Huang and C. Zhong, *Angew. Chem., Int. Ed.*, 2024, **63**, e202401770.
36 W. Xia, Z. Zhou, L. Sheng, L. Chen, F. Shen, F. Zheng, Z. Zhang, Q. Yang, Q. Ren and Z. Bao, *Nat. Commun.*, 2024, **15**, 8716.
37 J.-R. Li, R. J. Kuppler and H.-C. Zhou, *Chem. Soc. Rev.*, 2009, **38**, 1477–1504.
38 H. Wang and J. Li, *Acc. Chem. Res.*, 2019, **52**, 1968–1978.
39 X.-W. Zhang, D.-D. Zhou and J.-P. Zhang, *Chem*, 2021, **7**, 1006–1019.
40 H. Wang, Y. Liu and J. Li, *Adv. Mater.*, 2020, **32**, 2002603.
41 L. Li, J. G. Bell, S. Tang, X. Lv, C. Wang, Y. Xing, X. Zhao and K. M. Thomas, *Chem. Mater.*, 2014, **26**, 4679–4695.
42 B. Van de Voorde, B. Bueken, J. Denayer and D. De Vos, *Chem. Soc. Rev.*, 2014, **43**, 5766–5788.
43 W. R. Lee, D. W. Ryu, W. J. Phang, J. H. Park and C. S. Hong, *Chem. Commun.*, 2012, **48**, 10847–10849.
44 L. Yu, X. Dong, Q. Gong, S. R. Acharya, Y. Lin, H. Wang, Y. Han, T. Thonhauser and J. Li, *J. Am. Chem. Soc.*, 2020, **142**, 6925–6929.
45 L. Yu, S. Ullah, H. Wang, Q. Xia, T. Thonhauser and J. Li, *Angew Chem. Int. Ed. Engl.*, 2022, **61**, e202211359.
46 Y. W. Alsmeyer, W. V. Childs, R. M. Flynn, G. G. I. Moore and J. C. Smeltzer, *Electrochemical Fluorination and Its Applications*, Springer US, Boston, 1994.
47 CCDC 2544357: Experimental Crystal Structure Determination, 2026, DOI: 10.5517/ccdc.csd.cc2rdm1v.